ChemComm

COMMUNICATION

View Article Online
View Journal | View Issue

Cite this: *Chem. Commun.*, 2025, 61, 286

Received 18th October 2024,
Accepted 26th November 2024

DOI: 10.1039/d4cc05434b

rsc.li/chemcomm

Combining mechanical ball-milling with melt-polymerization to fabricate polyimide covalent organic frameworks towards high-performance sodium-ion batteries†

Yu Wu,[a] Xu Han,[b] Hailong Hu,[a] Hongyin Hu,[a] Jinyan Wang,[a] Yaoyao Deng,[c] Fang Duan,[a] Hongwei Gu,[b] Mingliang Du[a] and Shuanglong Lu*[a]

Melt-polymerization and mechanical ball-milling were combined to achieve the facile mass production of polyimide covalent organic frameworks (COFs) towards high-performance sodium-ion batteries. The as-obtained COFs were demonstrated with high utilization of active sites (>83.0%) and COFs with smaller pore sizes were proved to deliver better performance with a specific capacity of 213.7 mA h g^{-1} at a current density of 0.1 A g^{-1}.

Electrochemical energy storage technologies are vital to modern life, with secondary batteries extensively utilized across electronic devices, electric transportation, and aerospace sectors.[1,2] These technologies are crucial for the development of a sustainable and low-carbon society.[3] However, the escalating demand for lithium-ion batteries (LIBs) has led to concerns regarding the depletion of lithium resources and associated safety issues.[4] In response, the development of sodium-ion batteries (SIBs), noted for their safety and resource abundance, has emerged as a promising alternative to address these challenges. Among the various anode materials for SIBs, carbon-based materials are particularly promising due to their abundant resources, excellent sodium storage capacity and favourable electrochemical performance.[5] Covalent organic frameworks (COFs), emerging as porous organic polymers, offer numerous advantages such as abundant active sites, well-defined pore structures, high specific surface areas and stable frameworks. These properties endow COFs with exceptional ionic fast diffusion characteristics, resulting in long cycle life and stability in SIBs.[6] Similar to LIBs, organic functional groups, such as carbonyl, triazine, imine, pyrazine and pyrenoimidazole, were identified as active sites for SIBs.[7–10] Pradhan *et al.* first reported the use of COFs containing triazine and imine groups as electrode materials towards SIBs in 2018.[8] To increase the density of active sites, Chen *et al.* reported a nitrogen-rich TQBQ-COF, incorporating multiple carbonyl groups, for SIB applications. This COF, characterized by six carbonyl groups and twelve pyrazine groups within a single nanopore, exhibited a theoretical capacity of up to 515 mA h g^{-1}. However, at a current density of 0.1 A g^{-1}, the utilization of active sites was limited to 58.2%.[9] Apparently, in addition to increasing the density of active sites in COFs, improving their actual utilization is crucial for further enhancing battery performance.

To enable practical applications, the scalable and efficient production of COFs is also one of the important factors to be considered, as typical solvothermal synthesis usually involves an organic solvent and complex procedures. Recently, melt polymerization has emerged as a promising alternative for the large-scale production of COFs with high crystallinity. This solvent-free method offers key advantages, such as operational simplicity and environmental sustainability.[11,12] Zhang *et al.* successfully employed melt polymerization to synthesize a series of polyimide COFs, achieving significant advancements in gas storage and separation applications.[13] Furthermore, Zhang and colleagues employed this approach to construct a series of sp^2-COFs towards efficient photocatalysis through the Knoevenagel condensation reaction.[14] Despite various advantages of melt-polymerized COFs, it is noted that these COFs often display compact stacking structures, primarily due to strong interlayer π–π interactions. Moreover, in an example reported by Zhang *et al.*, COFs synthesized by solvothermal methods with an AA stacking conformation changed to an ABC stacking arrangement when synthesized by melt polymerization, which may further increase the stacking.[15]

Previous research has demonstrated that the insufficient active sites and prolonged ion diffusion within batteries may result from the densely packed structures of COFs. In the case of LIBs, Sun *et al.* found that the atomic-layer COFs, obtained through exfoliation using a ball-milling method, could significantly improve its specific

[a] *Key Laboratory of Synthetic and Biological Colloids, Ministry of Education, School of Chemical and Material Engineering, Jiangnan University, Wuxi, Jiangsu 214122, P. R. China. E-mail: lushuanglong@jiangnan.edu.cn*

[b] *Key Laboratory of Organic Synthesis of Jiangsu Province, College of Chemistry, Chemical Engineering and Materials Science, Collaborative Innovation Center of Suzhou Nano Science and Technology, Soochow University, Suzhou 215123, China*

[c] *School of Chemical Engineering and Materials Science, Changzhou Institute of Technology, Changzhou 213032, China*

† Electronic supplementary information (ESI) available: Experimental details, and more characterization. See DOI: https://doi.org/10.1039/d4cc05434b

capacity, from 25.1 mA h g^{-1} to 110 mA h g^{-1} at a current density of 0.2 A g^{-1} compared to the original bulk materials.[16] Similarly, the influence of stacking behavior in COFs on the performance of SIBs was also investigated by modulating the thickness of COF nanosheets. These findings indicate that the thinner COF nanosheets are conducive to enhancing their capacity contribution, thereby improving overall battery performance.[17] Therefore, taken together, developing scalable production methods for COFs that maximize active site utilization remains a significant challenge and an important area of ongoing research.

In this work, we combined melt-polymerization and mechanical ball-milling to achieve the facile mass production of polyimide COFs with high utilization of active sites towards high-performance SIBs. Two polyimide COFs, $COF_{PMA-TAPT}$ and $COF_{PMA-TTBT}$, constructed by pyromellitic acid (PMA) and 1,3,5-tris-(4-aminophenyl)triazine (TAPT) and 4,4,4-(1,3,5-triazine-2,4,6-triyl)-tris-(([1,1-biphenyl]-4-amine)) (TTBT) *via* melt-polymerization were selected for the investigation. The two COFs possess different pore sizes but identical carbonyl and triazine redox sites to interact with Na ions. The strong π–π interactions lead to a tighter COF structure and longer ion transport paths, which inhibit Na^+ migration at high charge/discharge rates, affecting the effective utilization of the redox active sites and ultimately leading to a decrease in capacity. After the subsequent mechanical ball-milling, downsized and thinner COF particles were achieved. Both COFs exhibited excellent electrochemical performance with high utilization of active sites (>83.0%). It is proved that $COF_{PMA-TAPT}$ with smaller pore sizes delivered better performance with a specific capacity of 213.7 mA h g^{-1} at a current density of 0.1 A g^{-1}. In addition, at a current density of 1 A g^{-1}, its specific capacity could remain at 147.3 mA h g^{-1} with a coulombic efficiency (CE) close to 100% after 1500 cycles, showing its excellent stability.

As illustrated in Fig. 1, the typical COFs with abundant imide linkages as active sites were synthesized through a two-step process. First, the COFs were prepared using benzoic acid as a flux, following previously established methods. Subsequently, the COFs were stripped by ball-milling. It is assumed that the stripped COFs may expose more active sites, while the reduced grain size may optimize the diffusion path of Na^+ and promote its rapid transport.

Their chemical structures are shown in Fig. 2a. Fourier transform infrared (FT-IR) spectroscopy confirms the successful synthesis of $COF_{PMA-TAPT}$ and $COF_{PMA-TTBT}$, evidenced by the imide bond C–N–C peaks at 1359 cm^{-1} and 1353 cm^{-1}, respectively. The absorption peaks at 1717 cm^{-1} and 1776 cm^{-1} are assigned to symmetric and

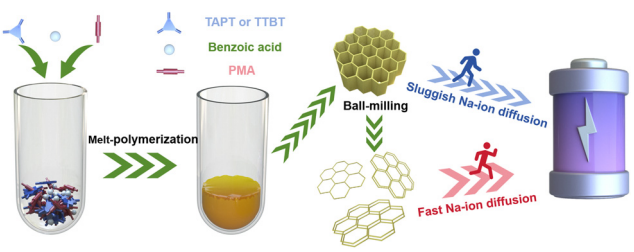

Fig. 1 Schematic illustration of the facile synthesis of downsized and thinner COF particles for SIBs.

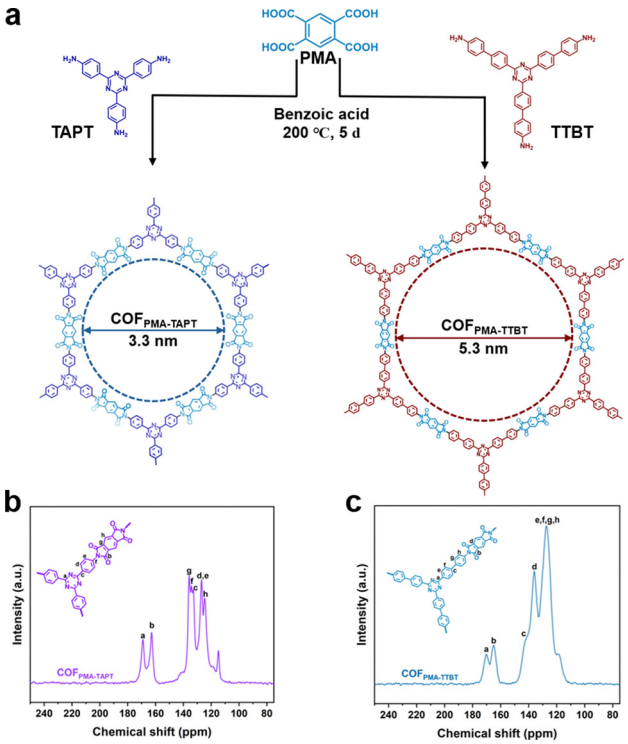

Fig. 2 (a) Chemical structures of $COF_{PMA-TAPT}$ and $COF_{PMA-TTBT}$. (b) and (c) Solid-state ^{13}C CP/MAS NMR spectra of $COF_{PMA-TAPT}$ and $COF_{PMA-TTBT}$, respectively.

asymmetric vibrations of the five-membered imide carbonyl group (Fig. S1a and b, ESI†). The solid-state ^{13}C cross polarization magic angle spinning nuclear magnetic resonance (^{13}C CP/MAS NMR) spectra for both COFs revealed a carbonyl (C═O) signal at 163 ppm and a triazinyl (N–C═N) carbon signal at 172 ppm, along with additional characteristic carbon signals consistent with their chemical structures (Fig. 2b and c). The XPS survey spectra (Fig. S2 and S3, ESI†) revealed that the elemental compositions of both COFs consisted of C, N, and O elements. Furthermore, the C 1s, N 1s, and O 1s (Fig. S2b–d and Fig. S3b–d, ESI†) spectra provided additional confirmation of the structural similarity between the synthesized $COF_{PMA-TAPT}$ and $COF_{PMA-TTBT}$. This ensures that the active sites are under identical conditions, facilitating an exploration of their performance differences.[16]

The crystal structures of the materials were characterized by powder X-ray diffraction (PXRD), along with structural simulations and Pawley refinement. Both COFs exhibit AA stacking arrangements. The optimized parameters for the unit cell of $COF_{PMA-TAPT}$ are $a = b = 36.35$ Å, $c = 3.48$ Å (residuals: $R_{wp} = 5.51\%$ and $R_p = 3.88\%$), and for $COF_{PMA-TTBT}$ are $a = b = 51.45$ Å, $c = 3.54$ Å (residuals: $R_{wp} = 3.27\%$ and $R_p = 2.40\%$). The diffraction peaks corresponding to the (100) planes of $COF_{PMA-TAPT}$ and $COF_{PMA-TTBT}$ are observed at 2.83° and 2.19°, respectively, with additional remarkable peaks, as shown in Fig. 3a and b. Apparently, both of them have superior crystallinity. The Brunauer–Emmett–Teller (BET) surface areas for $COF_{PMA-TAPT}$ and $COF_{PMA-TTBT}$ were determined to be 1985.3 m^2 g^{-1} and 505.9 m^2 g^{-1}, respectively (Fig. 3c and d). The analysis of the pore size distribution *via* nonlocal density functional theory (NLDFT)

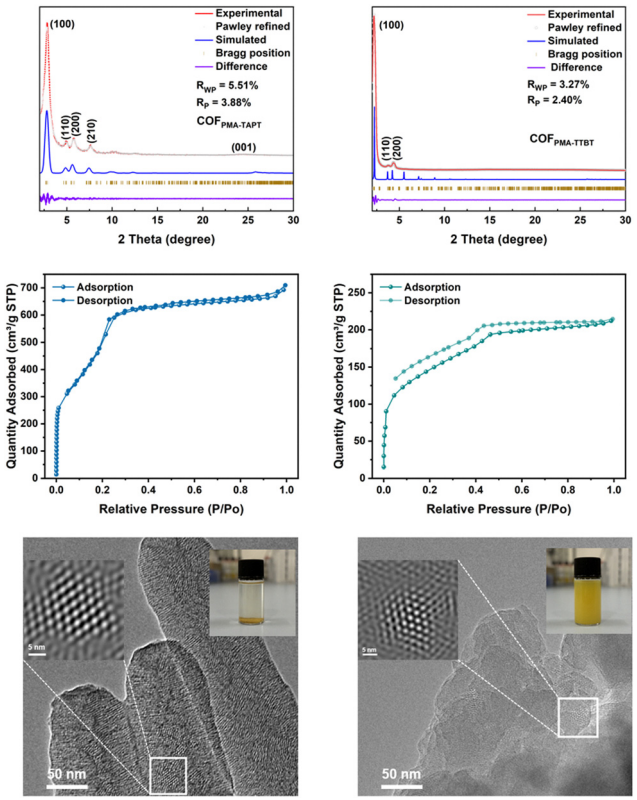

Fig. 3 (a) and (b) PXRD patterns of $COF_{PMA-TAPT}$ and $COF_{PMA-TTBT}$, respectively. (c) and (d) N_2 adsorption and desorption curves at 77 K of $COF_{PMA-TAPT}$ and $COF_{PMA-TTBT}$. (e) and (f) TEM image, HR-TEM image of $COF_{PMA-TAPT}$ and $COF_{PMA-TAPT}$ after mechanical ball-milling, respectively.

revealed the average pore size for $COF_{PMA-TAPT}$ (2.8 nm) and $COF_{PMA-TTBT}$ (3.7 nm) (Fig. S4a and b, ESI†). It is noteworthy that both of them are smaller than their theoretical pore sizes, which may have resulted from their highly compact stacking.[18]

To evaluate the stability of the COFs, their structural integrity and PXRD patterns were examined after immersion in different solvents for 48 hours, demonstrating their potential excellent stability in the subsequent processing procedures (Fig. S5, ESI†). Scanning electron microscopy (SEM) revealed that both COFs consisted of densely stacked blocks (Fig. S6a and b, ESI†). Their good crystallinities were further confirmed by transmission electron microscopy (TEM) images, as shown in Fig. 3e and Fig. S7a (ESI†). From the Fourier transformation (FFT) of a selected region in the TEM images, highly ordered structures and hexagonal tiling (hcb) networks within both COFs could be clearly illustrated. It should be noted that probably due to the highly dense stacking structures, it is hard for the ground power of as-obtained COFs to be well dispersed in solvents such as ethanol even after 1 hour of sonication (inset in Fig. 3e). However, after the subsequent treatment by mechanical ball-milling, the dispersion of the COF powder in solvent was significantly improved. As evidenced by the TEM images after the mechanical ball-milling, the crystalline structure of the $COF_{PMA-TAPT}$ could be well maintained, while downsized and thinner COF particles were achieved. Apparently, in addition to the enhanced dispersion in processing solvents, this morphology transformation could deliver higher contact area with Na ions, which is highly conductive to the higher utilization of active sites.[19]

We assembled CR 2032 coin cells using $COF_{PMA-TAPT}$ and $COF_{PMA-TTBT}$ as electrode materials and evaluated their electrochemical performance. The reversibility of the redox processes for both electrode materials was examined through cyclic voltammetry (CV) at a scan rate of 0.2 mV s^{-1} over five cycles. The results showed that, apart from the first cycle, during which the formation of a solid electrolyte interphase (SEI) layer was observed, the redox curves for the two materials were highly consistent across the subsequent four cycles. This high degree of overlap indicates excellent redox reversibility and cycling stability for both $COF_{PMA-TAPT}$ and $COF_{PMA-TTBT}$.

Analysis of the redox behavior reveals distinct peaks for $COF_{PMA-TTBT}$. A cathodic peak at 0.01 V (*vs.* Na/Na^+) in the CV profile of $COF_{PMA-TAPT}$ suggests the presence of Na^+ within its cavity. Subsequently, an anodic peak at 0.08 V during the forward scan indicates the reversible oxidation of reactive groups in $COF_{PMA-TAPT}$. The slight shift in redox peaks between the two materials can be attributed to differences in pore size, which would influence ion diffusion rates and electrochemical reaction kinetics, leading to the observed variations. Furthermore, the integrated area under the CV curve for $COF_{PMA-TAPT}$ (256 mA h g^{-1}) exceeds that of $COF_{PMA-TTBT}$ (187 mA h g^{-1}), reflecting a higher capacity in line with theoretical predictions (Fig. 4a, b and Scheme S1, ESI†). Comparative rate capability and long-cycling tests indicate that the performance of $COF_{PMA-TAPT}$ outperforms that of $COF_{PMA-TTBT}$. Specifically, at current densities of 0.1–5.0 A g^{-1}, $COF_{PMA-TAPT}$ exhibits capacities of 253.4, 230.2, 214.1, 196.8, 176.3, 159.4, 151.8 and 138.3 mA h g^{-1}, respectively. In contrast, $COF_{PMA-TTBT}$ shows capacities of 157.7, 143.2, 136.1, 130.5, 124.0, 117.1, 112.2 and 105.2 mA h g^{-1} under the same conditions (Fig. 4c and d). The decreasing difference in specific capacity between the two COFs at higher current densities can be explained by the rapid redox reactions of surface or near-surface carbonyl and triazine groups, which dominate at elevated current densities. Following the rate performance tests, stability evaluations conducted at 0.1 A g^{-1} showed that $COF_{PMA-TAPT}$ maintained a specific capacity of 213.7 mA h g^{-1}, outperforming $COF_{PMA-TTBT}$, which exhibited a capacity of 157.6 mA h g^{-1}. The utilization rates of the active sites were determined to be 83.5% for $COF_{PMA-TAPT}$ and 84.3% for $COF_{PMA-TTBT}$ (Fig. 4e). The batteries were subjected to a prolonged cycling test, consisting of 100 cycles at a current density of 0.1 A g^{-1} (Fig. S8a and b, ESI†). Both COFs demonstrated excellent stability, with coulombic efficiency (CE) consistently approaching 100%. Furthermore, after over 1500 cycles at a current density of 1 A g^{-1}, $COF_{PMA-TAPT}$ maintained a specific capacity of 147.3 mA h g^{-1}, with its CE remaining stable at 100% (Fig. S9, ESI†). These findings highlight the exceptional cycling stability and durability of polyimide COFs when employed as electrode materials.

The electrochemical reaction kinetics of the COF were evaluated using electrochemical impedance spectroscopy (EIS) (Fig. S10, ESI†). $COF_{PMA-TAPT}$ exhibited a lower R_2 value of 19.11 Ω compared to $COF_{PMA-TTBT}$ (45.61 Ω). This indicates that $COF_{PMA-TAPT}$ facilitates more efficient charge transfer. Additionally, the diffusion of Na^+ within the electrodes was assessed using the modified Warburg impedance (W_1), with values of 7.16 Ω for $COF_{PMA-TAPT}$ and 34.18 Ω

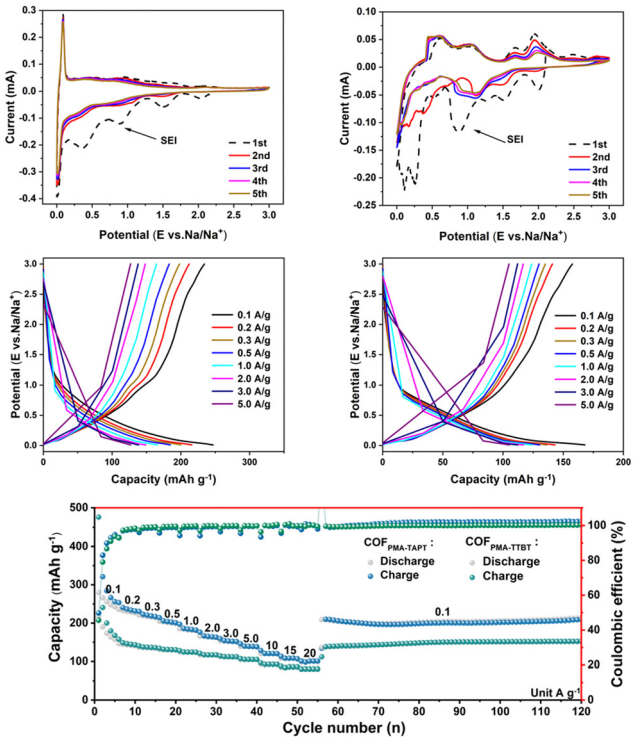

Fig. 4 (a) and (b) The CV plots of $COF_{PMA-TAPT}$ and $COF_{PMA-TTBT}$ were obtained at a scan rate of 0.2 mV s^{-1}. (c) and (d) The galvanostatic charge–discharge curves of $COF_{PMA-TAPT}$ and $COF_{PMA-TTBT}$ were measured over a current range from 0.1 A g^{-1} up to 5.0 A g^{-1}. (e) The rate performance of $COF_{PMA-TAPT}$ and $COF_{PMA-TTBT}$.

for $COF_{PMA-TTBT}$, further confirming that ion transport is more favorable in the smaller apertures of $COF_{PMA-TAPT}$ (Table S1, ESI†). Further analysis explored the de-sodiation and sodiation kinetics of $COF_{PMA-TAPT}$ using CV at various scan rates (0.2–1.0 mV s^{-1}). By examining the relationship between scan rate and peak current, the diffusion behavior and pseudocapacitive characteristics of the electrode materials during charge and discharge were assessed (Fig. S11a, ESI†). The value of b, derived from the equation $i = av^b$, was calculated through linear fitting of the redox peaks. The b values at the cathode and anode peaks were $P_{O1} = 0.53$, $P_{O2} = 0.83$, $P_{R1} = 0.75$, and $P_{R2} = 1.07$, respectively (Fig. S11b, ESI†). This suggests that the $COF_{PMA-TAPT}$ electrode material demonstrates a combination of battery-like and pseudo-capacitive behaviors. The contributions of pseudo-capacitance and diffusion were calculated using the equation $i(V) = k_1v + k_2^{1/2}$. Notably, the contribution of pseudocapacitance increased with the scan rate, reflecting enhanced electron transport and active site utilization (Fig. S11c, ESI†). These findings highlight the efficient electron transport and high utilization of active sites in $COF_{PMA-TAPT}$, contributing to its superior electrochemical performance.

In summary, we successfully developed a method to fabricate COFs for SIBs through the combination of melt polymerization and mechanical ball-milling. Two typical polyimide COFs with different pore sizes but identical carbonyl and triazine redox sites were prepared and investigated. It was proved that the downsized and thinner COF particles were favorable for the high utilization of active sites, thus enhancing their battery performance. Moreover, $COF_{PMA-TAPT}$ with smaller pore sizes and higher density of active sites was demonstrated to have better performance with a specific capacity of 213.7 mA h g^{-1} at a current density of 0.1 A g^{-1}. In addition, it could also show excellent stability. This approach shows advantages in the mass production of COFs with high utilization of active sites, which may provide a new avenue for the development of advanced SIBs in industrial applications.

This study was supported by the National Natural Science Foundation of China (NSFC) (52173201, 21905115) and the Fundamental Research Funds for the Central Universities (JUSRP622039).

Data availability

The data supporting this article have been included as part of the ESI.†

Conflicts of interest

There are no conflicts to declare.

Notes and references

1 S. Tan, Z. Shadike, X. Cai, R. Lin, A. Kludze, O. Borodin, B. L. Lucht, C. Wang, E. Hu, K. Xu and X. Q. Yang, *Electrochem. Energy Rev.*, 2023, **6**, 35.
2 K. Turcheniuk, D. Bondarev, G. G. Amatucci and G. Yushin, *Mater. Today*, 2021, **42**, 57–72.
3 W. Li, J. Liu and D. Zhao, *Nat. Rev. Mater.*, 2016, **1**, 16023.
4 H. Du, Y. Wang, Y. Kang, Y. Zhao, Y. Tian, X. Wang, Y. Tan, Z. Liang, J. Wozny, T. Li, D. Ren, L. Wang, X. He, P. Xiao, E. Mao, N. Tavajohi, F. Kang and B. Li, *Adv. Mater.*, 2024, **36**, 2401482.
5 S. Ma, W. Yan, Y. Dong, Y. Su, L. Ma, Y. Li, Y. Fang, B. Wang, S. Wu, C. Liu, S. Chen, L. Chen, Q. Huang, J. Wang, N. Li and F. Wu, *Mater. Today*, 2024, **75**, 334–358.
6 S.-W. Ke, W. Li, L. Gao, J. Su, R. Luo, S. Yuan, P. He and J.-L. Zuo, *Angew. Chem., Int. Ed.*, 2024, e202417493.
7 L. Liu, Y. Gong, Y. Tong, H. Tian, X. Wang, Y. Hu, S. Huang, W. Huang, S. Sharma, J. Cui, Y. Jin, W. Gong and W. Zhang, *CCS Chem.*, 2024, **6**, 1255–1263.
8 B. C. Patra, S. K. Das, A. Ghosh, A. Raj K, P. Moitra, M. Addicoat, S. Mitra, A. Bhaumik, S. Bhattacharya and A. Pradhan, *J. Mater. Chem. A*, 2018, **6**, 16655–16663.
9 R. Shi, L. Liu, Y. Lu, C. Wang, Y. Li, L. Li, Z. Yan and J. Chen, *Nat. Commun.*, 2020, **11**, 178.
10 M. Zhang, Y. Tong, Z. Sun, J. Wang, Y. Lin, F. Kang, Q. Zhang and W. Huang, *Chem. Mater.*, 2023, **35**, 4873–4881.
11 F. Meng, S. Bi, Z. Sun, D. Wu and F. Zhang, *Angew. Chem., Int. Ed.*, 2022, **61**, e202210447.
12 P. Zhang, Z. Wang, S. Wang, J. Wang, J. Liu, T. Wang, Y. Chen, P. Cheng and Z. Zhang, *Angew. Chem., Int. Ed.*, 2022, **61**, e202213247.
13 Z. Wang, Y. Zhang, T. Wang, L. Hao, E. Lin, Y. Chen, P. Cheng and Z. Zhang, *Chem*, 2023, **9**, 2178–2193.
14 M. Li, X. Chi, Z. Zhang, S. Bi, F. Meng, Y. Jiao, K. Mou, Z. Wang, B. Xue, X. Li and F. Zhang, *Angew. Chem., Int. Ed.*, 2024, e202411474.
15 Z. Wang, Y. Zhang, T. Wang, E. Lin, T. Wang, Y. Chen, P. Cheng and Z. Zhang, *Small*, 2023, **19**, 2303684.
16 G. Zhao, H. Li, Z. Gao, L. Xu, Z. Mei, S. Cai, T. Liu, X. Yang, H. Guo and X. Sun, *Adv. Funct. Mater.*, 2021, **31**, 2101019.
17 S. Gu, S. Wu, L. Cao, M. Li, N. Qin, J. Zhu, Z. Wang, Y. Li, Z. Li, J. Chen and Z. Lu, *J. Am. Chem. Soc.*, 2019, **141**, 9623–9628.
18 S. T. Emmerling, R. Schuldt, S. Bette, L. Yao, R. E. Dinnebier, J. Kästner and B. V. Lotsch, *J. Am. Chem. Soc.*, 2021, **143**, 15711–15722.
19 K. Endo, A. Raza, L. Yao, S. Van Gele, A. Rodríguez-Camargo, H. A. Vignolo-González, L. Grunenberg and B. V. Lotsch, *Adv. Mater.*, 2024, **36**, 2313197.